Two-Dimensional Lattice Boltzmann Model for Droplet Impingement and Breakup in Low Density Ratio Liquids

Amit Gupta[1] and Ranganathan Kumar[2,*]

[1] *Department of Mechanical Engineering, Indian Institute of Technology, New Delhi, India 110016.*
[2] *Department of Mechanical, Materials and Aerospace Engineering, University of Central Florida, Orlando, FL 32816, USA.*

Abstract. A two-dimensional lattice Boltzmann model has been employed to simulate the impingement of a liquid drop on a dry surface. For a range of Weber number, Reynolds number and low density ratios, multiple phases leading to breakup have been obtained. An analytical solution for breakup as function of Reynolds and Weber number based on the conservation of energy is shown to match well with the simulations. At the moment breakup occurs, the spread diameter is maximum; it increases with Weber number and reaches an asymptotic value at a density ratio of 10. Droplet breakup is found to be more viable for the case when the wall is non-wetting or neutral as compared to a wetting surface. Upon breakup, the distance between the daughter droplets is much higher for the case with a non-wetting wall, which illustrates the role of the surface interactions in the outcome of the impact.

AMS subject classifications: 76T10

Key words: Lattice Boltzmann, droplet impingement, spread factor, breakup.

1 Introduction

Impingement of liquid droplets onto a dry surface can be observed in natural and modern engineering phenomenon such as rain drops on the surface of the earth, atomized fuel on the piston of an internal combustion engine, in ink-jet printing, spray cooling and recently in microfabrication [1]. A variety of mechanisms underlying the impact of liquid droplets on a dry surface, and the subsequent spreading behavior, have been

---

*Corresponding author. *Email addresses:* `agupta@mech.iitd.ac.in` (A. Gupta), `Ranganathan.Kumar@ucf.edu` (R. Kumar)

highlighted through a variety of experimental investigations [2–10]. The breakup of the parent droplet into daughter droplets, and the difference in the dynamics of a single drop impact with a dry wall as compared to that of a train of drops has been demonstrated as well [4]. Scheller and Bousfield [5] showed that the contact angle effect on the spreading film diameter is negligible for droplet $Re > 10$, and that the maximum spread factor follows the correlation given by

$$\zeta_{\max} = 0.61(Re^2 Oh)^{0.166}. \tag{1.1}$$

Rioboo et al. [6] showed that during the receding process, the perturbations merge leading to a rebound of the droplet for the case of water drops impacting a wax surface. However, for cases where no rebound was noticed, the diameter of the spreading film either remained constant or increased depending on the wettability of the surface used.

In addition to the experimental work, droplet impact dynamics has also been the subject of considerable numerical investigations [11–16]. However, much of the numerical work has been focused on simulations of droplet impingement on a surface covered with a thin liquid film [11–15]. Using the volume-of-fluid (VOF) method, Josserand and Zaleski [11] developed a criterion to scale the transition between splashing and deposition of liquid droplets on a thin liquid film. The VOF method has also been employed to identify the conditions leading to the entrapment of vapor bubbles as a result of capillary wave formed as a result of the droplet impact [12]. Lee and Lin [13] have developed and applied a high density ratio lattice Boltzmann model to simulate the splashing and deposition of droplets on a thin film. Mukherjee and Abraham [14,15] extended the earlier model [13] to simulate the deposition and splashing behavior for an axi-symmetric domain. In a separate study, droplet spreading behavior for very low Oh and subsequent rebound on a dry surface for low density ratios was also investigated [16].

Impact of a droplet on a dry surface may be vastly different from that on a thin film, and is likely to be dependent on the density ratio of the two fluids, especially in high pressure systems where the parameter has a low value. The final shape and spreading of the liquid drop also depends on a range of parameters, like the impact velocity (U), the size of the droplet (D), the angle of attack to the surface, the physical properties of the liquid drop and the surrounding pressure.

The objective of this work is to (a) illustrate the applicability of a two-dimensional lattice Boltzmann method (LBM) in simulating droplet impingement on a dry surface, (b) to elucidate the mechanisms involved in the collision and subsequent relaxation of liquid droplets, and (c) to identify the physics of droplet breakup mechanism for low density ratios. Based on the conservation of energy, a criterion based on Reynolds number, Weber number, and the density ratio is developed to predict whether the collision of a liquid droplet would result in its breakup into daughter droplets. In addition, the physical behavior as a result of droplet collision may depend on whether the surface is hydrophobic or hydrophilic, rough or smooth, and dry or wet. This work also briefly explores the effect of the interaction between a liquid and the wetting characteristics (hydrophilic or hydrophobic) of a surface, and its influence on the breakup process.

2 Lattice Boltzmann method

In recent years, LBM has emerged as a powerful alternative to study the fluid behavior in problems relating to two-phase and porous media flows [17,18]. LBM requires no empirical correlations for the closure of extra source terms in the governing equations, and at the same time can yield detailed physics of the flow around single or multiple droplets. The interface is no longer a mathematical boundary; it is a post-processed quantity that can be detected by monitoring the variation in fluid densities.

The Boltzmann's kinetic equation describes the evolution of the single particle distribution function ($f_i(\mathbf{x},t)$) as a function of space and time. Unlike conventional schemes that are based on discretization of continuum based macroscopic equations, LBM models the kinetic equations. These simplified kinetic models incorporate the nature of physics at the microscale such that the flow field variables obey the macroscopic governing equations.

The lattice Boltzmann equation for the evolution of the particle distribution function can be written as

$$f_i(\mathbf{x}+\mathbf{e}_i\delta t,t+\delta t)=f_i(\mathbf{x},t)-\frac{f_i(\mathbf{x},t)-f_i^{eq}(\mathbf{x},t)}{\tau},\qquad i=0,1,\cdots,b-1,\qquad(2.1)$$

where the particular form of the collision operator with the single time relaxation approximation, also known as the lattice BGK (Bhatnagar-Gross-Krook) operator has been used. In this work, the two-dimensional, nine-speed, phase-space discretization model, D2Q9, for the discrete velocity space has been used that gives a square lattice for the space discretization. The velocity vectors are given as

$$\mathbf{e}_i=\begin{cases}(0,0), & i=0,\\(\pm1,0)c,\ (0,\pm1)c, & i=1,2,3,4,\\(\pm1,\pm1)c, & i=5,6,7,8.\end{cases}\qquad(2.2)$$

The macroscopic density and the macroscopic momentum density at each lattice are defined in terms of the particle distribution functions by

$$\rho=\sum_i f_i=\sum_i f_i^{eq},\qquad \rho\mathbf{u}=\sum_i f_i\mathbf{e}_i=\sum_i f_i^{eq}\mathbf{e}_i.\qquad(2.3)$$

The equilibrium distribution functions depend only on local density and velocity and are given as:

$$f_i^{eq}=\frac{\rho-d_0}{b}+\frac{\rho D}{c^2b}(\mathbf{e}_i\cdot\mathbf{u})+\rho\frac{D(D+2)}{2c^4b}(\mathbf{e}_i\mathbf{e}_i:\mathbf{u}\mathbf{u})-\frac{\rho D}{2c^2b}(\mathbf{u}\cdot\mathbf{u}),\qquad(2.4a)$$

$$f_0^{eq}=d_0-\frac{\rho}{c^2}(\mathbf{u}\cdot\mathbf{u}),\qquad(2.4b)$$

where f_i^{eq} is the equilibrium distribution of particles moving in direction i, f_0^{eq} is the equilibrium distribution of rest particles, D is the dimension rank (2 for two-dimensions),

b is the number of lattice directions, c is the lattice unit length, and d_0 is the average rest particle number [19]. The lattice Boltzmann's equation bridges the gap between the microscopic and macroscopic fluid interactions as it yields the Navier-Stokes equation in the low Mach number limit using the Chapman-Enskog expansion [17,18], and is second order accurate in space. In addition, $\tau > 1/2$ in order for viscosity to be positive.

2.1 Multiphase model in LBM

LBM has been shown to be especially useful for the simulation of multiphase flows due to its local nature and the solution of a linear equation to determine the macroscopic fluid behavior. As a result, a number of different variants have been proposed to conduct multiphase simulations in the domain of this method [13–16, 20–29]. One of the earliest and commonly used methods is the Shan-Chen's (S-C) model [21]. Hou et al. [22] have compared the chromodynamic [20] and the S-C [21] models and showed that the latter was superior by recording the pressure and velocity at the interface of a static bubble equilibrated in a three-dimensional domain. The two models were also reported to suffer from some shortcomings, such as high spurious velocities at the interface, and their inability to simulate high density ratio fluids. A recent improvement of the chromodynamic model [27] has been proposed to counter the problem of high spurious velocities at the interface; however, the model could only work for fluids with equal densities [30,31]. Despite these shortcomings, the S-C model has been widely used to simulate multiphase flows with low to moderate density ratios in a variety of recent studies because of its ease of implementation and isotropic nature of solutions [28, 29, 32–34, 36, 38].

Since the current study is focused on droplet interactions at high pressures and low density ratios, the S-C model has been adopted. The S-C model incorporates non-local interactions among particles to simulate multiple component fluids. The interaction potential between components σ and $\bar{\sigma}$ is defined as

$$V(\mathbf{x},\mathbf{x}') = G_{\sigma\bar{\sigma}}(\mathbf{x},\mathbf{x}')\psi^{\sigma}(\mathbf{x})\psi^{\bar{\sigma}}(\mathbf{x}'), \tag{2.5}$$

where $G_{\sigma\bar{\sigma}}(\mathbf{x},\mathbf{x}')$ is the Green's function. The quantity ψ^{σ} is the "effective mass" function, and for the case when with nearest neighbor interactions only, can be written as

$$G_{\sigma\bar{\sigma}}(\mathbf{x},\mathbf{x}') = \begin{cases} 0, & |\mathbf{x}-\mathbf{x}'| > c, \\ G_{\sigma\bar{\sigma}}, & |\mathbf{x}-\mathbf{x}'| = c. \end{cases} \tag{2.6}$$

The strength of the interaction between components σ and $\bar{\sigma}$ is quantified by the magnitude of the Green's function $(G_{\sigma\bar{\sigma}})$, while its sign determines whether the interaction is attractive or repulsive. As a result, the net force due to surface tension-based interaction at each lattice site can be written as

$$\mathbf{F}_{\text{int}}^{\sigma}(\mathbf{x}) = -\psi^{\sigma}(\mathbf{x}) \sum_{\bar{\sigma}=1}^{S} G_{\sigma\bar{\sigma}} \sum_{a=0}^{b-1} \psi^{\bar{\sigma}}(\mathbf{x}+\mathbf{e}_a)\mathbf{e}_a. \tag{2.7}$$

Similarly, at the solid-fluid interface, an attractive or repulsive force [35] could be incorporated to control the wetting nature of the heavier liquid with the solid surface. This form of the interaction is given by

$$\mathbf{F}^{\sigma}_{\text{wall}}(\mathbf{x}) = -\rho^{\sigma}(\mathbf{x}) \sum_{a=0}^{b-1} G_{w,\sigma} \rho^{\bar{\sigma}}(\mathbf{x}+\mathbf{e}_a)\mathbf{e}_a, \tag{2.8}$$

where the interaction parameter $G_{w,\sigma}$ denotes the intensity of interaction from the wall and the sign (positive/negative) indicates whether the interaction is repulsive/attractive (non-wetting/wetting). For the D2Q9 lattice used in this work, $G_{w,\sigma}$ takes into consideration the nearest and second-nearest nodes through the following equation,

$$G_{w,\sigma}(\mathbf{x},\mathbf{x}') = \begin{cases} G_w, & |\mathbf{x}-\mathbf{x}'|=1, \\ \dfrac{G_w}{4}, & |\mathbf{x}-\mathbf{x}'|=\sqrt{2}, \\ 0, & \text{otherwise.} \end{cases} \tag{2.9}$$

An external force of gravity is directed in the negative vertical direction. This external force can be introduced into the force equation using the expression [36]

$$\mathbf{F}^{\sigma}_{\text{ext}} = \rho^{\sigma}\mathbf{a}_{\text{ext}} = \rho^{\sigma}\mathbf{g}\left(1-\frac{\langle\rho\rangle}{\rho}\right), \tag{2.10}$$

where ρ is the mixture number density at the node of interest and $\langle\rho\rangle$ is the average number density of the mixture in the entire domain. Eq. (2.10) ensures that the average value of the external force is zero in the periodic domain, and hence the mass-average velocity of the mixture remains constant. Combining (Eqs. (2.7), (2.8) and (2.10), the total force at each lattice node can be computed by

$$\mathbf{F}^{\sigma}_{\text{tot}} = \mathbf{F}^{\sigma}_{\text{int}} + \mathbf{F}^{\sigma}_{\text{wall}} + \mathbf{F}^{\sigma}_{\text{ext}}. \tag{2.11}$$

The total force is incorporated into the momentum change at each node through the equilibrium distribution function before the collision step [37], such that

$$\rho^{\sigma}\mathbf{u}^{\sigma} = \rho^{\sigma}\mathbf{u} + \tau^{\sigma}\mathbf{F}^{\sigma}_{\text{tot}}(\mathbf{x}), \tag{2.12}$$

where

$$\rho^{\sigma} = m^{\sigma}f^{\sigma}(\mathbf{x}) \tag{2.13}$$

is the mass density of the σth component and

$$\mathbf{u} = \left(\sum_{\sigma}m^{\sigma}\sum_{a}f^{\sigma}_a\mathbf{e}_a/\tau^{\sigma}\right)\left(\sum_{\sigma}m^{\sigma}\sum_{a}f^{\sigma}_a/\tau^{\sigma}\right)^{-1} \tag{2.14}$$

and

$$f^{\sigma}(\mathbf{x}) = \sum_{a}f^{\sigma}_a. \tag{2.15}$$

3   Results and discussion

The S-C model [21] was first validated for simulation of bubbly flows using periodic boundary conditions. The drag force was calculated and the bubble shape regimes were found to match well with the experimentally observed shapes [38].

Droplet equilibration was conducted to generate a good initial condition in a channel with top and bottom boundaries as walls and side boundaries to be periodic. The upper boundary condition was changed from no-slip to free-slip, without significant difference in the diameter of the spreading film for results presented in later sections of this study. The nearest neighbor SC model [39] has been incorporated by including the next-nearest neighbor in the force discretization. Thus, Eq. (2.6) was modified to account for the second nearest neighbors as well, through the following modification,

$$G_{\sigma\bar{\sigma}}(\mathbf{x},\mathbf{x}') = \begin{cases} g, & |\mathbf{x}-\mathbf{x}'|=1, \\ \frac{g}{4}, & |\mathbf{x}-\mathbf{x}'|=\sqrt{2}, \\ 0, & \text{otherwise.} \end{cases} \tag{3.1}$$

The non-ideal equation of state for the fluid can then be written as

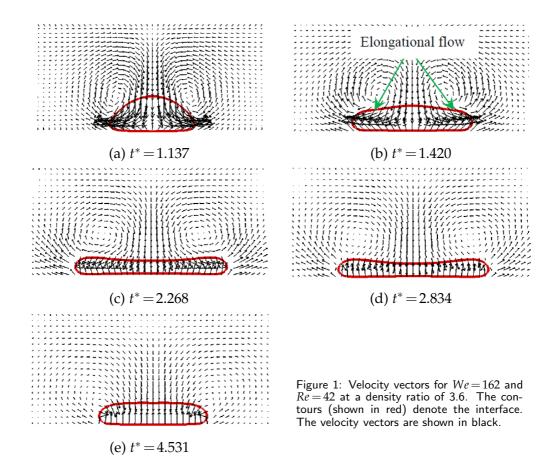$$p = c_S^2 \rho + \frac{3}{2} g \Psi^2(\rho), \tag{3.2}$$

where $c_S = 1/\sqrt{3}$ is the speed of sound in lattice units. A lower value of the interaction strength (i.e., $g < g_{\text{crit}} = -4/(9\rho_0)$) would result in phase separation of the liquid phase, and hence leads to a high density ratio. The "effective mass" function, Ψ, as given in the original work [21] was used.

$$\Psi(\rho) = \rho_0 \left[1 - \exp\left(-\frac{\rho}{\rho_0}\right) \right]. \tag{3.3}$$

The computational domain was divided into 400×100 lattice points, which was tested to be adequate to resolve the thinnest regions of the spreading lamella on the wall.

The important dimensionless parameters that classify the dynamics of droplet impact on a dry surface are the Weber number ($We = \rho_l U^2 D/\sigma$), Reynolds number ($Re = \rho_l UD/\mu_l$), and the spread factor (given by the ratio of the diameters of the film and the droplet (i.e., $\xi = d/D$)). The fluid-interaction parameter g, as given in Eq. (3.1), was varied between -0.047 to -0.054, and the corresponding density ratio in the simulations ranged from 4 and 10. The suspended droplet, whose radius was varied between 8 to 25 lattice units, was equilibrated for 20,000 lattice time steps such that the pressure inside and outside the drop converged to a steady state value. After the equilibration period, the external force was switched on and the drop was allowed to fall towards the solid surface.

Fig. 1 shows the results for droplet spreading on a surface for a density ratio of $\rho_l/\rho_g = 3.6$ at $We = 162$ and $Re = 42$. Non-dimensionalization of time was done using the

(a) $t^* = 1.137$

(b) $t^* = 1.420$

(c) $t^* = 2.268$

(d) $t^* = 2.834$

(e) $t^* = 4.531$

Figure 1: Velocity vectors for $We = 162$ and $Re = 42$ at a density ratio of 3.6. The contours (shown in red) denote the interface. The velocity vectors are shown in black.

characteristic time $t_{ref} = D/U$. The non-dimensionalized time at which each snapshot has been taken after the point of impact with the surface are also shown in the figure. A few observations can be made: after the droplet falls on the surface, it spreads and oscillates until it gets stretched to a maximum diameter (Figs. 1(a)-(c)), beyond which the contact line recedes in a non-uniform fashion (Fig. 1(e)). It can be seen that the droplet spreading process is quicker in the spreading phase in which the drop spreads due to an elongational flow after colliding with the surface. The velocity vectors around the droplet are shown at the appropriate time instants. Fig. 1(b) shows the presence of an elongational flow as the droplet undergoes the spreading phase. In this stage, the velocity of the heavier phase in the transverse (horizontal) direction drives it faster to an extremum (Fig. 1(c)) at $t^* = 2.268$. As a result of the drag on the lighter phase induced by the movement of the liquid film, a vortical flow is generated near the interface of the two phases, as is shown in Figs. 1(b) and (c). The strength of these vortices decreases with time as the spreading film dissipates momentum into the surrounding fluid. In Fig. 1(d), the shape of the droplet at the initiation of the relaxation phase is shown. In this phase, interfacial tension comes into play leading to the retraction of the interface. The relaxation to the final equilibrium

shape was found to take a longer amount of time as compared to the other phases of the process. Eventually, the drop attains a steady shape beyond which there is no significant change.

Simulations were done for a range of Weber and Reynolds numbers, but the ratio $We^{0.5}/Re$, called the Ohnesorge number (Oh), was held constant, to study the effect of the interplay of the viscous and surface tension forces on the spreading behavior of a single drop. Ohnesorge number is a measure of the viscous force relative to the surface tension force for a given size of the droplet. The time evolution of the spread factor ($\xi = d/D$) for $Oh = 0.197$ and different Weber numbers is shown in Fig. 2. For each We, the time evolution can be divided into four phases, (a) kinematic, (b) spreading, (c) relaxation, and (d) equilibrium. The spreading length was calculated based on the number of lattice points that are in contact with the heavier fluid at the wall. The physics of each phase is discussed below.

Assuming that the diameter of the drop after the impact is still the same, a simple expression for the spread factor, given as $\xi = d/D = 2t^{*1/2}$, where $t^* = tU/D$ can be obtained for a two-dimensional droplet in the kinematic phase ($t^* \ll 1$). The constant of proportionality was found to be 2.8 in experiments [6]. In the kinematic phase, the spread factor does not change significantly for different We and Re. The curve fit for the current LBM simulations in the kinematic phase of several cases yields $d/D = 1.42t^{*0.5}$ which compares reasonably well with the theoretical expression.

As the spreading phase begins, the velocity of the droplet in the transverse (horizontal) direction drives it faster to an extremum, as is shown in Fig. 1(b). Other parameters such as the diameter of the impacting droplet, the velocity, the surface tension and viscosity start to influence the rate at which the lamella spreads. Results of simulations conducted for a constant Oh are shown in Fig. 2. As can be observed, the spread factor is a strong function of We and Re which control the maximum diameter and time to reach an equilibrium shape, respectively. For the lowest Weber number of 2.78, the droplet diameter does not exceed the original diameter in any of the phases, and behaves similar to a rigid body. From Fig. 2, two observations on the relative influence of lowering the surface tension (i.e., increase of We) can be made: a) the peak diameter is reached after a much longer time, and b) the spread factor increases, reaching a maximum for $We = 140$. The effect of Reynolds number on the relaxation phase is shown in Fig. 3. Simulations conducted by increasing Re, while keeping We constant, showed that the droplet reached the final equilibrium shape at higher t^* values. A higher Re indicates lower viscous dissipation of the oscillating film into the surrounding lighter fluid.

Earlier experiments [8] have indicated that droplet spreading and breakup mechanism are a strong function of the surrounding density (or pressure). Fig. 4 shows that, for the constant We and Re, the spread factor is higher for the case with the higher density ratio. The spread factor was also found to be higher for wetting wall as compared to a non-wetting wall. A similar conclusion was also reached earlier [6] where experiments were conducted at $We > 35$. At a higher density ratio, the relaxation phase is marked by the presence of higher amplitude oscillations in the spreading diameter as is shown in
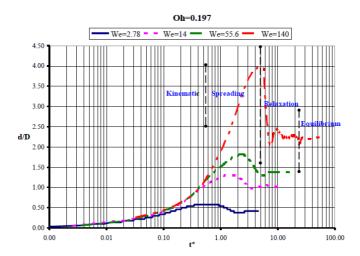
Figure 2: Time evolution of spread factor as a function of time for Ohnesorge number, Oh, $(We^{0.5}/Re)=0.197$.
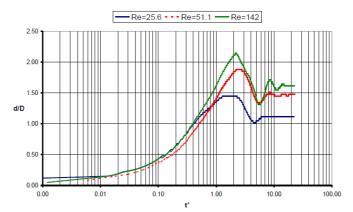

Figure 3: Spread factor variation for three different Re values at $We=21$. At higher Re, the oscillations in the relaxation phase are found to be higher compared to lower Re.
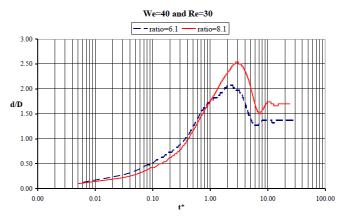

Figure 4: Comparison of spreading profiles for two different density ratios at $We=40$ and $Re=30$.

Fig. 4, which is also the case for $Re > 100$. These are attributed to (a) lower drag when the surrounding gas has a lower density, and (b) slower viscous dissipation of the receding drop when the surrounding gas has a lower viscosity, both of which lead to longer fluctuations in the attainment of the equilibrium shape of the spreading drop.

3.1 Droplet breakup analysis

An impinging droplet can breakup into smaller drops at higher Weber and Reynolds numbers. By the principle of conservation of energy before and after the impact,

$$E_{KE}^i + E_{PE}^i + E_{SE}^i = E_{KE}^f + E_{PE}^f + E_{SE}^f + E_{D}^f, \tag{3.4}$$

where E_{KE}^i, E_{PE}^i and E_{SE}^i are the kinetic, potential and surface energies before the impact of the liquid drop with the solid, and E_{KE}^f, E_{PE}^f, E_{SE}^f and E_{D}^f are the kinetic, potential, surface and dissipation energies after the impact [9]. For a two-dimensional drop of length L, the kinetic energy of impact can be written as

$$E_{KE}^i = \frac{1}{2}\Delta\rho U^2\left(\frac{\pi}{4}D^2 L\right), \tag{3.5}$$

where $\Delta\rho = \rho_l - \rho_g$ is the difference in densities of the two fluids. The thickness of the film (h) when the drop reaches a maximum diameter of D_{max} can be written as

$$\frac{\pi}{4}D^2 L = D_{max}hL \Rightarrow h = \frac{\pi}{4}\frac{D}{\zeta_{max}}, \tag{3.6}$$

where ζ_{max} is the ratio of the maximum film diameter to the initial diameter of the drop.

From [10], the dissipation energy can be simplified as

$$E_D \approx V\Phi t_e, \tag{3.7}$$

where Φ is the dissipation function, i.e.,

$$\Phi = \mu\left(\frac{\partial u_i}{\partial x_j} + \frac{\partial u_j}{\partial x_i}\right)\frac{\partial u_i}{\partial x_j},$$

which can be simplified to the form given by

$$\Rightarrow \Phi \approx \mu\left(\frac{U}{h}\right)^2, \tag{3.8}$$

$t_e = D/U$ is the time taken by the droplet height to go from D to 0. Thus, the dissipation energy is given by

$$E_D^f = \mu\left(\frac{U}{h}\right)^2\frac{D}{U}\left(\frac{\pi}{4}D^2 L\right) = \frac{4}{\pi}\mu UDL\zeta_{max}^2. \tag{3.9}$$

The surface energy before the impact is given by

$$E_{\text{SE}}^i = \sigma DL. \tag{3.10}$$

The surface energy at the instant when the maximum diameter $(D_{\max})$ is attained is given by

$$E_{\text{SE}}^f = \sigma D_{\max} L(1-\cos\theta). \tag{3.11}$$

For flows where $Re > 10$, it has been shown that the maximum spread factor does not depend on the contact angle. Moreover, analytical work [7] has also shown the minimal effect of capillary forces for flows with $We \gg Re^{1/2}$. Thus, the contact angle dependence on the surface energy is ignored. Back substituting into Eq. (3.4), and on simplification, the energy equation can be reduced to

$$\frac{8}{\pi}\frac{(\xi_{\max}-1)}{We} + \frac{32}{\pi^2}\frac{\xi_{\max}^2}{Re} = \frac{\Delta\rho}{\rho_l}. \tag{3.12}$$

For large differences in density, the right hand side of Eq. (3.12) would approach a constant value (i.e., $\Delta\rho/\rho_l \approx 1$). However, for the density ratios simulated in the current study, $\Delta\rho/\rho_l$ can vary from 0.75 to 0.9.

Due to the competition between the surface and kinetic energies, a liquid droplet undergoing spreading on a dry surface may breakup into daughter droplets. The energy analysis has been motivated by the need to quantify the interplay between the two. Thus, (3.12) can be used to predict the outcome of droplet impingement on a dry surface. The droplet will spread to a maximum diameter and breakup into smaller daughter droplets if

$$\frac{\rho_l}{\Delta\rho}\left(\frac{8}{\pi}\frac{(\xi_{\max}-1)}{We} + \frac{32}{\pi^2}\frac{\xi_{\max}^2}{Re}\right) < 1.$$

For situations where the following condition, given by

$$\frac{\rho_l}{\Delta\rho}\left(\frac{8}{\pi}\frac{(\xi_{\max}-1)}{We} + \frac{32}{\pi^2}\frac{\xi_{\max}^2}{Re}\right) > 1$$

is satisfied, the spreading film will relax to the final equilibrium shape without breaking into smaller droplets.

Using LBM results, a complete analysis of the 2D droplet breakup can be performed for a range of We and Re at different density ratios to observe a possible breakup of the parent drop into daughter droplets due to impact and surface interactions from the wall. For a density ratio that ranged from 3 to 10, the Weber and Reynolds number were increased linearly by increasing the diameter of the impacting drop without changing any of the other variables. The size of the domain in the transverse and longitudinal directions was correspondingly increased to between 8 and 10 times the diameter of the impinging drop to obtain grid independent solutions. The current multiphase model

Table 1: LBM simulation results at breakup for different density ratios.

Case	ρ_l/ρ_g	We	Re	ζ_{max}
(a)	3	347.85	75.13	3.7
(b)	4	330	91.1	4.637
(c)	5	252.08	97.56	5.01
(d)	6	222.21	103.87	5.21
(e)	8	186.85	115.57	5.83
(f)	10	183.91	132.1	6.1

precludes any changes in the surface tension parameter once the interaction strength $G_{\sigma\bar{\sigma}}$ is fixed. As the diameter is increased, the maximum film length also increases. At a critical value of Re and We, the drop breaks into daughter droplets when the maximum spreading diameter is reached. This process was repeated for other density ratios as well, and the results for We_{crit} and Re_{crit} are listed in Table 1, and plotted in Fig. 5. It can be observed that as the density ratio is increased, the maximum spread factor at breakup also increases, reaching an asymptote at a density ratio of 10. Using the density ratio and the Re_{crit} and We_{crit} values, the maximum spread factor at breakup can be back-calculated from the quadratic Eq. (3.12). The ζ_{max} obtained from Eq. (3.12) is compared with the actual ζ_{max} obtained from the LBM simulations, and is plotted in Fig. 6. For comparison, a line at 45° is drawn that corresponds to an exact match of LBM with theory. The LBM results and the solution from the energy equation were found to be accurate within a $\pm5\%$ error margin.
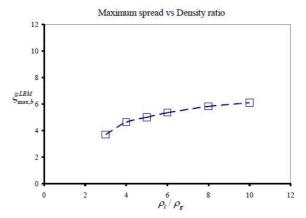

Figure 5: Plot with variation of maximum spread factor from LBM simulations at the moment of breakup as a function of density ratio for two-dimensional droplets.

The results of increasing We and Re for different density ratios are shown in Fig. 7. First, Re and We were increased by increasing the drop diameter for each density ratio until breakup occurred. The Weber number and Reynolds number were recorded at the point of breakup and used in (3.12) to find the maximum spread factor. Through this
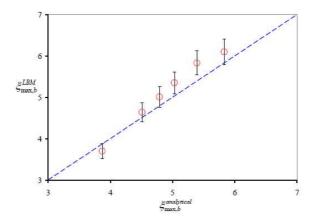
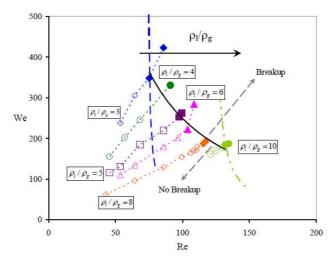Figure 6: Comparison of LBM results and the analytical solution from (3.12) for two-dimensional droplets.

Figure 7: The spread/breakup regime map for impact of single droplet with a solid surface for neutral wetting conditions. The hollow symbols indicate that droplet spreads without breakup, and the filled circles indicate a breakup of the parent droplet. The demarcating curves (broken lines) that are shown are from the solution of the equation $\frac{\rho_l}{\Delta \rho} \left(\frac{8}{\pi} \frac{(\xi_{\max}-1)}{We} + \frac{32}{\pi^2} \frac{\xi_{\max}^2}{Re} \right) = 1$ for selected density ratios of 3 (- - -) and 10 ($\cdots$). These curves move to the right as the density ratio is increased from 3 to 10. Also shown is the locus (solid line) of the critical parameters at breakup.

point, the breakup curve for the given density ratio was drawn. For example, at a density ratio of 3 and $\xi_{\max} = 3.7$ (see Table 1), a map of the possible outcomes given by $11/We + 73/Re = 1$ is shown in the figure. Similarly, for $\rho_l/\rho_g = 10$ and $\xi_{\max} = 6.1$, the analogous curve is given by $14/We + 122/Re = 1$ and is also shown in the figure. Consequently, the critical points at which breakup would occur fall in between these two curves. As the density ratio is increased, these curves shift to the right, decreasing and increasing the value of Weber and Reynolds number for breakup respectively. Several density ratios

were run to generate We_{crit} and Re_{crit}, and the locus of these points is drawn as the solid curve in Fig. 7. Below this critical line, droplet breakup would not occur, and above it, it would for any density ratio. Above We_{crit} and Re_{crit}, the drop may break into two to three smaller droplets.

3.2 Surface wetting characteristics of a 2D droplet

Wetting characteristics play an important role in determining the mechanism of breakup. Simulations were conducted at different Weber and Reynolds numbers, with different density ratios, to compare the effect of the wetting nature on possible breakup of the spreading liquid film on the wall. For $We = 114$ and $Re = 152$, the surface was varied to be wetting, neutral and non-wetting, as is shown in the Fig. 8. For a non-wetting surface (Fig. 8(c)), the impinging drop was observed to breakup readily impact with the solid surface. Since the surface is non-wetting, the drop fails to have an affinity for the solid wall, and in turn the surface interactions from the solid reduce the surface energy. This leads to a strong elongation flow and a high kinetic energy in the direction of spread, eventually leading to a breakup of the parent drop. In the case of a wetting surface, the surface energy is high, and thus plays a prominent role in reducing the kinetic energy
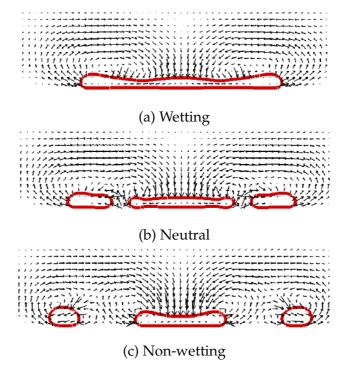

(a) Wetting

(b) Neutral

(c) Non-wetting

Figure 8: Different outcomes of a droplet splashing mechanism depending on the surface wetting characteristics at $We = 114$ and $Re = 152$. The domain size has been shown as truncated on the left and right boundaries and extends much further than as depicted.

in the transverse direction, due to which the film spreads to a maximum diameter and yet does not break into daughter drops (Fig. 8(a)). A neutral surface can be described by (3.12), and for the *We* and *Re*, as shown in Fig. 8(b), the outcome lies on the right of this critical curve. It can be observed that the nature of breakup of the spreading film is vastly different for the non- and neutral-wetting cases.

Thus, the wetting characteristics of the wall influence the geometric separation of the smaller droplets when the original drop eventually breaks up on the wall. Upon breakup, the distance between the daughter droplets is much higher for the case with a non-wetting wall as compared to breakup at a wetting wall. Hence, a possible breakup of the drop on a neutral or non-wetting surface can be averted by altering the surface and making it wetting in nature.

4   Conclusions

In this work, two-dimensional simulations of droplet impact dynamics using S-C model, that allows two-phase fluid-fluid and fluid-solid interactions, have been conducted. Simulations were performed with different densities of the heavier and lighter phases such that the density ratio lies between 3 and 10. For this range of density ratio, a breakup criterion based on a simplified energy conservation analysis was developed and validated with the aid of lattice Boltzmann method.

Several simulations of single-drop collisions on a dry wall were done for a range of Weber number $(2 < We < 162)$ and Reynolds number $(10 < Re < 100)$. The spread factor was shown be a strong function of the Weber number, which determines the maximum diameter of the spreading film, and the Reynolds number, which controls the time it takes for the droplet to reach the equilibrium shape. For $We =$ constant, simulations indicate that the time taken by the droplet to reach a final equilibrium shape increases as *Re* increases. A higher *Re* indicates lower viscous dissipation of the oscillating film into the surrounding lighter fluid. The role of the density ratio on the droplet spreading behavior was also recorded. In the relaxation phase, a higher density ratio results in higher amplitude oscillations in the spreading film diameter.

Criteria for two-dimensional droplet breakup was developed, which depends on *Re* and *We*. For a wide range of *Re* and *We*, the LBM simulations obeyed the droplet breakup criteria developed in this paper. The breakup of the droplet was observed to occur only after a maximum spread factor was reached. This value increased with the density ratio, but reached an asymptote at a density ratio of 10. The LBM simulation results were compared with an analytical solution for the spread factor based on the conservation of energy and were found to be within $\pm 5\%$ error margin.

The spreading behavior of the drops was also found to be a strong function of the wetting characteristics of the wall, although for impacts with high inertia the role of the wall wetting characteristics was not very significant as for low inertia impacts. Droplet breaks up readily for the case when the wall is non-wetting or neutral as compared to a

wetting surface. In addition, after the breakup on a non-wetting wall, the smaller droplets move farther away from each other. Such behavior illustrates the role of the surface interactions in the outcome of the impact. Hence, use of a hydrophilic surface can assist in delaying/averting the break-up on a liquid droplet impacting on a dry surface.

Nomenclature

a	acceleration	b	number of lattice directions
c	lattice unit length	c_s	speed of sound
d	diameter of the spreading film	D	diameter of the spherical drop
f	particle distribution function	F	force
G	Green's function	h	film thickness
m	molecular mass	p	pressure/momentum
r	radius of the drop	Re	Reynolds number$=\rho_l UD/\mu$
S	number of phases	t	time
u	velocity	U	drop impact velocity
V	interaction potential	We	Weber number$=\rho_l U^2 D/\sigma$
e_i	lattice speed of particles moving in direction i		
g	acceleration due to gravity/fluid-fluid interaction strength		
Oh	Ohnesorge number$=\mu/(\rho\sigma D)^{1/2}=We^{1/2}/Re$		

Greek symbols

ρ	density	σ	surface tension
μ	dynamic viscosity	ν	kinematic viscosity
τ	relaxation time	ξ	spread factor
θ	contact angle	$\delta_{\alpha\beta}$	Kronecker delta
ψ	effective mass function	Ψ	dissipation function

Subscripts

crit	critical	D	dissipation
e	effective	ext	external
g	gas	i	index
int	interaction	KE	kinetic energy
l	liquid	max	maximum
PE	potential energy	ref	reference
SE	surface energy	sph	sphere
tot	total	w	wall
σ	phase index		

Superscripts

$*$	non-dimensional quantities	eq	equilibrium
f	final	i	initial
σ	phase index		

References

[1] A. L. Yarin, Drop impact dynamics: splashing, spreading, receding, bouncing $\cdots$, Ann. Rev. Fluid Mech., 38 (2006), 159–192.

[2] L. H. J. Wachters and N. A. J. Westerling, The heat transfer from a hot wall to impinging water drops in the spheroidal state, Chem. Eng. Sci., 21 (1966), 1047–1056.

[3] C. D. Stow and M. G. Hadfield, An experimental investigation of fluid flow resulting from the impact of a water drop with an unyielding dry surface, Proc. R. Soc. Lond. A, 373 (1981), 419–441.

[4] A. L. Yarin and D. A. Weiss, Impact of drops on solid surfaces: self-similar capillary waves, and splashing as a new type of kinematic discontinuity, J. Fluid Mech., 283 (1995), 141–173.

[5] B. L. Scheller and D. W. Bousfield, Newtonian drop impact with a solid surface, AIChE J., 41 (1995), 1357–1367.

[6] R. Rioboo, M. Marengo and C. Tropea, Time evolution of liquid drop impact onto solid, dry surfaces, Expt. Fluids, 33 (2002), 112–124.

[7] M. Pasandideh-Fard, Y. M. Qiao, S. Chandra and J. Mostaghimi, Capillary effects during droplet impact on a solid surface, Phys. Fluids, 8 (1996), 650–659.

[8] L. Xu, W. W. Zhang and S. R. Nagel, Drop splashing on a dry smooth surface, Phys. Rev. Lett., 94 (2005), 184505.

[9] C. Mundo, M. Sommerfeld and C. Tropea, Droplet-wall collisions: experimental studies of the deformation and breakup process, Int. J. Multiphase Flow, 21 (1995), 151–173.

[10] S. Chandra and C. T. Avedisian, On the collision of a droplet with a solid surface, Proc. R. Soc. Lond. A, 432 (1991), 13–41.

[11] C. Josserand and S. Zaleski, Droplet splashing on a thin liquid film, Phys. Fluids, 15 (2003), 1650–1657.

[12] D. Morton, M. Rudman and L. Jong-Leng, An investigation of the flow regimes resulting from splashing drops, Phys. Fluids, 12 (2000), 747–763.

[13] T. Lee and C.-L. Lin, A stable discretization of the lattice Boltzmann equation for simulation of incompressible two-phase flows at high density ratio, J. Comput. Phys., 206 (2005), 16–47.

[14] S. Mukherjee and J. Abraham, Lattice Boltzmann simulations of two-phase flow with high density ratio in axially symmetric geometry, Phys. Rev. E, 75 (2007), 026701.

[15] S. Mukherjee and J. Abraham, Crown behavior in drop impact on wet walls, Phys. Fluids, 19 (2007), 052103.

[16] S. Mukherjee and J. Abraham, Investigations of drop impact on dry walls with a lattice-Boltzmann model, J. Coll. Inter. Sci., 312 (2007), 341–354.

[17] R. Benzi, S. Succi and M. Vergassola, The lattice Boltzmann equation: theory and applications, Phys. Rep., 222 (1992), 145–197.

[18] S. Succi, The Lattice Boltzmann Equation for Fluid Dynamics and Beyond, Oxford University Press, 2001.

[19] D. R. Noble, S. Chen, J. G. Georgiadis and R. O. Buckius, A consistent hydrodynamic boundary condition for the lattice Boltzmann method, Phys. Fluids, 7 (1995), 203–209.

[20] D. Rothman and J. Keller, Immiscible cellular-automaton fluids, J. Stat. Phys., 52 (1988), 1119–1127.

[21] X. Shan and H. Chen, Lattice Boltzmann model for simulating flows with multiple phases and components, Phys. Rev. E, 47 (1993), 1815–1819.

[22] S. Hou, X. Shan, Q. Zou, G. D. Doolen and W. E. Soll, Evaluation of two lattice Boltzmann models for multiphase flows, J. Comput. Phys., 138 (1997), 695–713.

[23] M. Swift, W. Osborne and J. Yeomans, Lattice Boltzmann simulation of nonideal fluids, Phys. Rev. Lett., 75 (1995), 830–833.

[24] T. Inamuro, S. Tajima and F. Ogino, Lattice Boltzmann simulation of droplet collision dynamics, Int. J. Heat Mass Trans., 47 (2004), 4649–4657.

[25] I. O. Kurtoglo and C. L. Lin., Lattice Boltzmann simulation of bubble dynamics, Num. Heat Trans. B, 50 (2006), 333–351.

[26] X. He, S. Chen and R. Zhang, A lattice Boltzmann scheme for incompressible multiphase flow and its application in simulation of Rayleigh-Taylor instability, J. Comput. Phys., 152 (1999), 642–663.

[27] S. V. Lishchuk, C. M. Care and I. Halliday, Lattice Boltzmann algorithm for surface tension with greatly reduced microcurrents, Phys. Rev. E, 67 (2003), 036701.

[28] G. Falcucci, G. Bella, G. Chiatti, S. Chibbaro, M. Sbragaglia and S. Succi, Lattice Boltzmann models with mid-range interactions, Commun. Comput. Phys., 1 (2006), 1–13.

[29] G. Falcucci, S. Chibbaro, S. Succi, X. Shan and H. Chen, Lattice Boltzmann spray-like fluids, Europhys. Lett., 82 (2008), 24005.

[30] A. Gupta, S. M. S. Murshed and R. Kumar, Droplet formation and stability of flows in a microfluidic T-junction, Appl. Phys. Lett., 94 (2009), 164107.

[31] A. Gupta and R. Kumar, Effect of geometry on droplet formation in the squeezing regime in a microfluidic T-junction, Microfluidics Nanofluidics, 8 (2010), 799–812.

[32] Q. Kang, D. Zhang and S. Chen, Displacement of a two-dimensional immiscible droplet in a channel, Phys. Fluids, 14 (2002), 3203–3214.

[33] Q. Kang, D. Zhang and S. Chen, Displacement of a three-dimensional immiscible droplet in a duct, J. Fluid Mech., 545 (2005), 41–66.

[34] H. Huang, D. T. Thorne, M. G. Schaap and M. C. Sukop, Proposed approximation for contact angles in Shan-and-Chen-type multicomponent multiphase lattice Boltzmann models, Phys. Rev. E, 76 (2007), 066701.

[35] N. S. Martys and H. Chen, Simulation of multicomponent fluids in complex three-dimensional geometries by the lattice Boltzmann method, Phys. Rev. E, 53 (1996), 743–750.

[36] K. Sankaranarayanan, X. Shan, I. G. Kevrekidis and S. Sundaresan, Analysis of drag and virtual mass forces in bubbly suspensions using an implicit formulation of the lattice Boltzmann method, J. Fluid Mech., 452 (2002), 61–96.

[37] J. M. Buick and C. A. Greated, Gravity in a lattice Boltzmann model, Phys. Rev. E, 61 (2000), 5307–5320.

[38] A. Gupta and R. Kumar, Lattice Boltzmann simulation to study multiple bubble dynamics, Int. J. Heat Mass Trans., 51 (2008), 5192–5203.

[39] P. Yuan and L. Schaefer, Equations of state in a lattice Boltzmann model, Phys. Fluids, 18 (2006), 042101.